Closing the gap between Earth-based and interplanetary mission observations: Vesta seen by VLT/SPHERE

Romain Jl. Fétick, Laurent Jorda, Pierre Vernazza, Michael Marsset, Alexis Drouard, Thierry Fusco, Benoît Carry, Franck Marchis, Josef Hanuš, Matti Viikinkoski, et al.

Astronomy & Astrophysics manuscript no. output
November 30, 2018

Closing the gap between Earth-based and interplanetary mission observations: Vesta seen by VLT/SPHERE $\star$,$\star\star$

R. JL. Fétick[1], L. Jorda[1], P. Vernazza[1], M. Marsset[2,3], A. Drouard[1], T. Fusco[1,4], B. Carry[5], F. Marchis[6], J. Hanuš[7], M. Viikinkoski[8], M. Birlan[9], P. Bartczak[10], J. Berthier[9], J. Castillo-Rogez[11], F. Cipriani[12], F. Colas[9], G. Dudziński[10], C. Dumas[13], M. Ferrais[14], E. Jehin[14], M. Kaasalainen[8], A. Kryszczynska[10], P. Lamy[1], H. Le Coroller[1], A. Marciniak[10], T. Michalowski[10], P. Michel[5], L.M. Mugnier[4], B. Neichel[1], M. Pajuelo[9,15], E. Podlewska-Gaca[10,16], T. Santana-Ros[10], P. Tanga[5], F. Vachier[9], A. Vigan[1], O. Witasse[12], and B. Yang[17]

[1] Aix Marseille Univ, CNRS, LAM, Laboratoire d'Astrophysique de Marseille, Marseille, France
*e-mail: `romain.fetick@lam.fr`
[2] Department of Earth, Atmospheric and Planetary Sciences, MIT, 77 Massachusetts Avenue, Cambridge, MA 02139, USA
[3] Astrophysics Research Centre, Queen's University Belfast, BT7 1NN, UK
[4] ONERA, The French Aerospace Lab BP72, 29 avenue de la Division Leclerc, 92322 Chatillon Cedex, France
[5] Université Côte d'Azur, Observatoire de la Cote d'Azur, CNRS, Laboratoire Lagrange, France
[6] SETI Institute, Carl Sagan Center, 189 Bernado Avenue, Mountain View CA 94043, USA
[7] Institute of Astronomy, Charles University, Prague, V Holešovičkách 2, CZ-18000, Prague 8, Czech Republic
[8] Department of Mathematics, Tampere University of Technology, PO Box 553, 33101, Tampere, Finland
[9] IMCCE, Observatoire de Paris, 77 avenue Denfert-Rochereau, F-75014 Paris Cedex, France
[10] Astronomical Observatory Institute, Faculty of Physics, Adam Mickiewicz University, Słoneczna 36, 60-286 Poznań, Poland
[11] Jet Propulsion Laboratory, California Institute of Technology, 4800 Oak Grove Drive, Pasadena, CA 91109, USA
[12] European Space Agency, ESTEC - Scientific Support Office, Keplerlaan 1, Noordwijk 2200 AG, The Netherlands
[13] TMT Observatory, 100 W. Walnut Street, Suite 300, Pasadena, CA 91124, USA
[14] Space sciences, Technologies and Astrophysics Research Institute, Université de Liège, Allée du 6 Août 17, 4000 Liège, Belgium
[15] Sección Física, Departamento de Ciencias, Pontificia Universidad Católica del Perú, Apartado, Lima 1761, Perú
[16] Institute of Physics, University of Szczecin, Wielkopolska 15, 70-453 Szczecin, Poland
[17] European Southern Observatory (ESO), Alonso de Cordova 3107, 1900 Casilla Vitacura, Santiago, Chile

July 2018

ABSTRACT

Context. Over the past decades, several interplanetary missions have studied small bodies *in situ*, leading to major advances in our understanding of their geological and geophysical properties. Such missions, however, are limited in number of targets. Among them, the NASA Dawn mission has characterised in detail the topography and albedo variegation across the surface of asteroid (4) Vesta, down to a spatial resolution of ∼20 m/pixel scale.

Aims. Here, we aimed at determining how much topographic and albedo information can be retrieved from the ground with VLT/SPHERE in the case of Vesta, having a former space mission (Dawn) providing us with the ground truth that can be used as benchmark.

Methods. We observed Vesta with VLT/SPHERE/ZIMPOL as part of our ESO large program (ID 199.C-0074) at six different epochs, and deconvolved the collected images with a parametric Point Spread Function (PSF). We then compared our images with synthetic views of Vesta generated from the 3D shape model of the Dawn mission, on which we projected Vesta's albedo information.

Results. We show that the deconvolution of the VLT/SPHERE images with a parametric PSF allows retrieving the main topographic and albedo features present across the surface of Vesta, down to a spatial resolution of ∼20–30 km. Contours extraction shows an accuracy of ∼1 pixel (3.6 mas).

Conclusions. The present study provides the very first quantitative estimate of the accuracy of ground-based adaptive-optics imaging observations of asteroid surfaces. In the case of Vesta, the upcoming generation of 30-40 m-sized telescopes (ELT, TMT, GMT) should in principle be able to resolve all of the main features present across its surface, including the troughs and the North-South crater dichotomy, provided that they operate at the diffraction limit.

Key words. Techniques: high angular resolution – Techniques: image processing – Methods: observational – Minor planets, asteroids: individual: (4) Vesta

* Based on observations made with ESO Telescopes at the Paranal Observatory under program ID 199.C-0074 (PI: P. Vernazza)
** As soon as papers for our large program are accepted for publication, we make the corresponding reduced and deconvolved AO images and 3D shape models publicly available at http://observations.lam.fr/astero/.

1. Introduction

The surface topography of Vesta, the second largest main belt asteroid after the dwarf planet Ceres, has been characterised in detail by the framing camera (FC) on board the NASA Dawn mission. The Dawn FC mapped ∼80% of Vesta's surface with image scales of ∼20 m/pixel. These images revealed a complex topography (Russell et al. 2012; Jaumann et al. 2012; Marchi et al. 2012; Schenk et al. 2012) summarised below:

- The south polar region consists of two overlapping impact basins (Rheasilvia & Veneneia) and a central mound whose height rivals that of Olympic Mons on Mars. Part of the outer perimeter of the Rheasilvia basin is delimited by a steep scarp. Note that both the impact basin and the central peak were first detected by Thomas et al. (1997) using the Hubble Space Telescope.
- The surface is characterised by regions with elevated topography (∼20 km) such as the so-called Vestalia Terra whose southernmost part merges into the rim area of the Rheasilvia basin (Jaumann et al. 2012).
- Numerous troughs are present across Vesta's surface, especially in the equatorial and northern regions. Equatorial troughs have lengths that vary from 19 to 380 km, and can be as wide as 15 km whereas the most prominent northern trough is 390 km long and 38 km wide (Jaumann et al. 2012).
- Vesta's cratering record shows a strong north-south dichotomy with Vesta's northern terrains being significantly more cratered than the southern ones (Marchi et al. 2012).

The images of the Dawn mission also allowed producing a high-resolution map of the albedo across Vesta's surface, revealing the greatest variation of geometric albedo of any asteroid yet observed (the geometric albedo varies between ∼0.15 and ∼0.6; Reddy et al. 2012; Schröder et al. 2014).

Here, we present a new set of ground based images of Vesta acquired with VLT/SPHERE/ZIMPOL as part of our ESO large program (ID 199.C-0074; Vernazza et al. 2018). These observations were performed with the aim to test, through direct comparison with the Dawn *in situ* measurements: (i) the accuracy of the images acquired with this new-generation Adaptive-Optics (AO) system (Beuzit et al. 2008; Fusco et al. 2006, 2016), as well as (ii) the robustness of our deconvolution algorithm which uses a synthetic Point Spread Function (PSF) as input. These observations were also used to determine which of the geologic features discovered by Dawn (see above) can already be identified from the ground, and to place a size limit above which these features can be retrieved. Finally, these observations were used to produce an albedo map that could be directly compared with that based on the images of the Dawn FC (Schröder et al. 2014). In summary, Vesta was used as benchmark target for our large program, allowing us to test and ultimately validate our different techniques of image analysis.

2. Observations and data reduction

We observed (4) Vesta with the VLT/SPHERE/ZIMPOL instrument (Beuzit et al. 2008; Thalmann et al. 2008; Schmid et al. 2012) at six different epochs between May 20^{th}, 2018 and July 10^{th}, 2018 (see Table A.1 for a complete list of the observations). The data reduction protocol is the same for all the targets of our large program. We refer the reader to Vernazza et al. (2018) for a description of the procedure. A subset of the Vesta images after pipeline reduction and before deconvolution are shown in Fig. B.1.

3. Deconvolution method

3.1. Recurrent deconvolution artefacts with the observed PSF

Our large program was initially designed as follows. Each asteroid observation was followed by the acquisition of a stellar PSF, using a star of same apparent magnitude as the asteroid. The asteroid image and its associated PSF were then fed to the MISTRAL algorithm (Mugnier et al. 2004) for the deconvolution process. It appeared that for nearly 50% of the observations, the deconvolution resulted in strong artefacts at the asteroid edges, highlighted by the presence of a bright corona (see upper left panel of Fig. 2 as an example). Note that edge issues resulting from the deconvolution process have already been reported in the literature (Marchis et al. 2006).

The problem was slightly improved using myopic deconvolution (Conan et al. 1998) with the MISTRAL algorithm. In this mode, the gradient-descent algorithm estimates simultaneously the couple {object+PSF}. Specifically, the PSF observed during the night was used to compute an average Optical Transfer Function (OTF), that is, the Fourier transform of the PSF, and all the PSFs observed during the large program were used to compute a variance of the OTF around the average. Using this approach, the artefact intensity was reduced but still visible. This seemed to indicate that the deconvolution issues came from the PSF itself. We further inferred that the deconvolution artefacts may arise from a mismatch between the observed stellar PSF, and the intrinsic one during the asteroid observation. Indeed, if the shape of the observed PSF is too far from that of the true PSF, the myopic deconvolution cannot completely correct this issue. Moreover, myopic (or blind) deconvolution estimates simultaneously the asteroid image and the PSF, leading to an optimisation process depending on a large number of parameters. Each extra parameter *degenerates* the minimisation process. Reducing the number of parameters for the PSF is thus critical to avoid *degeneracy* and deconvolution issues.

3.2. Use of a parametric PSF for the deconvolution

To overcome the deconvolution issues we faced, we started using parametric PSFs instead of the stellar ones. The advantage of a parametric PSF lies in the flexibility of its parameters, which can be adjusted to better estimate the true underlying PSF during our asteroid observation. We chose to model these synthetic PSFs using a Moffat-shape profile (Moffat 1969), as such functions are widely used in astronomy to reproduce the sharp coherent peak and wide

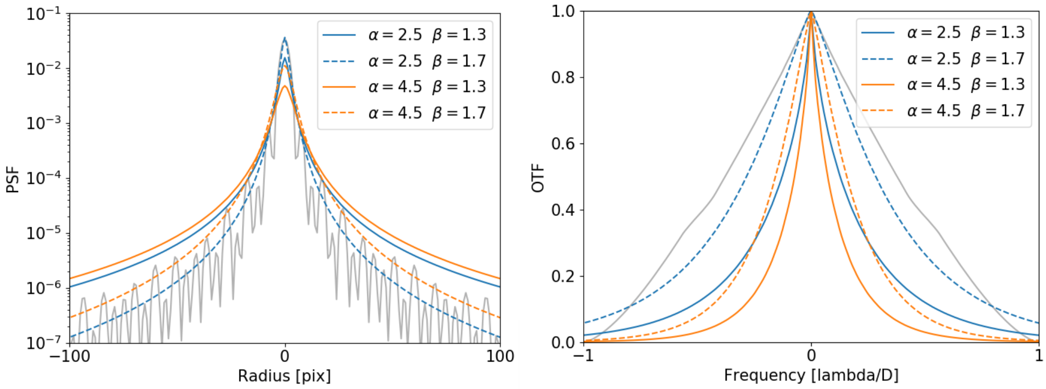

Fig. 1: 4 of the 25 Moffat PSFs (left) used for deconvolution, and their associated OTF (right). Colors indicate different values of α, and line styles show different values of β. Gray curves in the left and right panels are respectively the PSF and OTF representing the diffraction limit of the SPHERE 8m pupil at $\lambda = 646$ nm.

wings of PSFs in AO observations (Andersen et al. 2006; Sánchez et al. 2006). Additionally the Moffat function has also the advantage that it depends on two parameters only. It is defined as

$$M(r) = \frac{\beta - 1}{\pi\alpha^2} \frac{1}{(1 + r^2/\alpha^2)^{\beta}} \quad (1)$$

where r is the radius to the PSF centre, α is a scale factor, and β is the Moffat power law index. Setting $\beta > 1$ is necessary to have a finite energy. Under this condition, the multiplicative factor $(\beta - 1)/\pi\alpha^2$ in the expression ensures the total PSF energy is equal to unity.

As a next step, we allowed the two Moffat parameters α and β to vary within their realistic range of values, that is, $(\alpha, \beta) \in \,]0, +\infty[\, \times \,]1, +\infty[$. We then determined a reasonable range of values from a visual inspection of the images: $(\alpha, \beta) \in [2.5, 4.5] \times [1.3, 1.7]$, where α is given in pixels. Figure 1 shows 4 of the 25 Moffat PSFs tested for the deconvolution of our Vesta images (for respectively the minimum and the maximum values of α and β), and highlights what we consider to be a large range of PSF shapes for the deconvolution process.

After scanning the full range of α and β, two systematic trends were identified among the deconvolved Vesta images: i) a large α value in tandem with a small β value leads to the corona artefact that regularly occured using observed PSFs (see 3.1) and ii) a small α value in tandem with a large β value leads to "under-deconvolution", meaning that the image blurring is only partially attenuated and the deconvolution is not complete (see Fig. 2).

Theses trends can be physically well understood when considering the fact that the Full-Width-Half-Maximum (FWHM) and Strehl ratio of the Moffat PSF are function of α and β, where the FWHM can be written as

$$\text{FWHM} = 2\alpha\sqrt{2^{1/\beta} - 1} \quad (2)$$

and the Strehl ratio as

$$\text{Strehl ratio} = \frac{M(0)}{A(0)} = \frac{\beta - 1}{\pi\alpha^2} \frac{1}{A(0)} \quad (3)$$

with $A(0)$ being the diffraction pattern induced by the pupil (the Airy pattern for a circular non-obstructed aperture) at the center of the PSF $r = 0$.

The diagonal behaviour observed for the deconvolution with respect to the α and β parameters (Fig. 2) makes sense when looking at the corresponding PSFs' FWHM and Strehl ratios in Fig. 2 (bottom figure). For large FWHMs (upper-left corner) – or equivalently low Strehl ratios – deconvolution artefacts appear (corona artefact). This implies that the corona artefacts we encountered during the deconvolution process with observed PSFs most likely occured either because the observed PSFs were over-estimating the FWHM of our asteroid observations or under-estimating their Strehl ratio. Inversely, for small FWHMs – large Strehl ratios – the Vesta images appear "under-deconvolved". The bottom-left to upper-right diagonal shows rather stable values for both the FWHM and the Strehl ratio, in agreement with the deconvolution visual quality highlighted in Fig. 2. Given the deconvolution trend as a function of the Strehl ratio (Fig. 2), we always choose α and β parameters such as the object's edges were as sharp as possible without reaching the point where the bright corona effect appears (Strehl ratio of 20-30% in Fig. 2). This method has already been applied to the images acquired for (16) Psyche (Viikinkoski et al. 2018) and is now systematically applied to all targets within our large program. In the present case, a quantitative justification (i.e. the accuracy of our deconvolved Vesta images with respect to those of the Dawn mission) for the choice of the (α, β) parameters is given in Sec.4.5.

In summary, the deconvolution with a Moffat PSF converges in practice toward satisfactory results. Within our large program, we therefore started systematically using a parametric PSF with a Moffat shape to deconvolve our images. The deconvolved images of Vesta are shown in Figs. 3.

4. VLT/SPHERE compared to Dawn

In this section, we determine how much topographic and albedo information can be retrieved from the ground with VLT/SPHERE in the case of Vesta, having a former space mission (Dawn) providing us with the ground truth that we can use as benchmark.

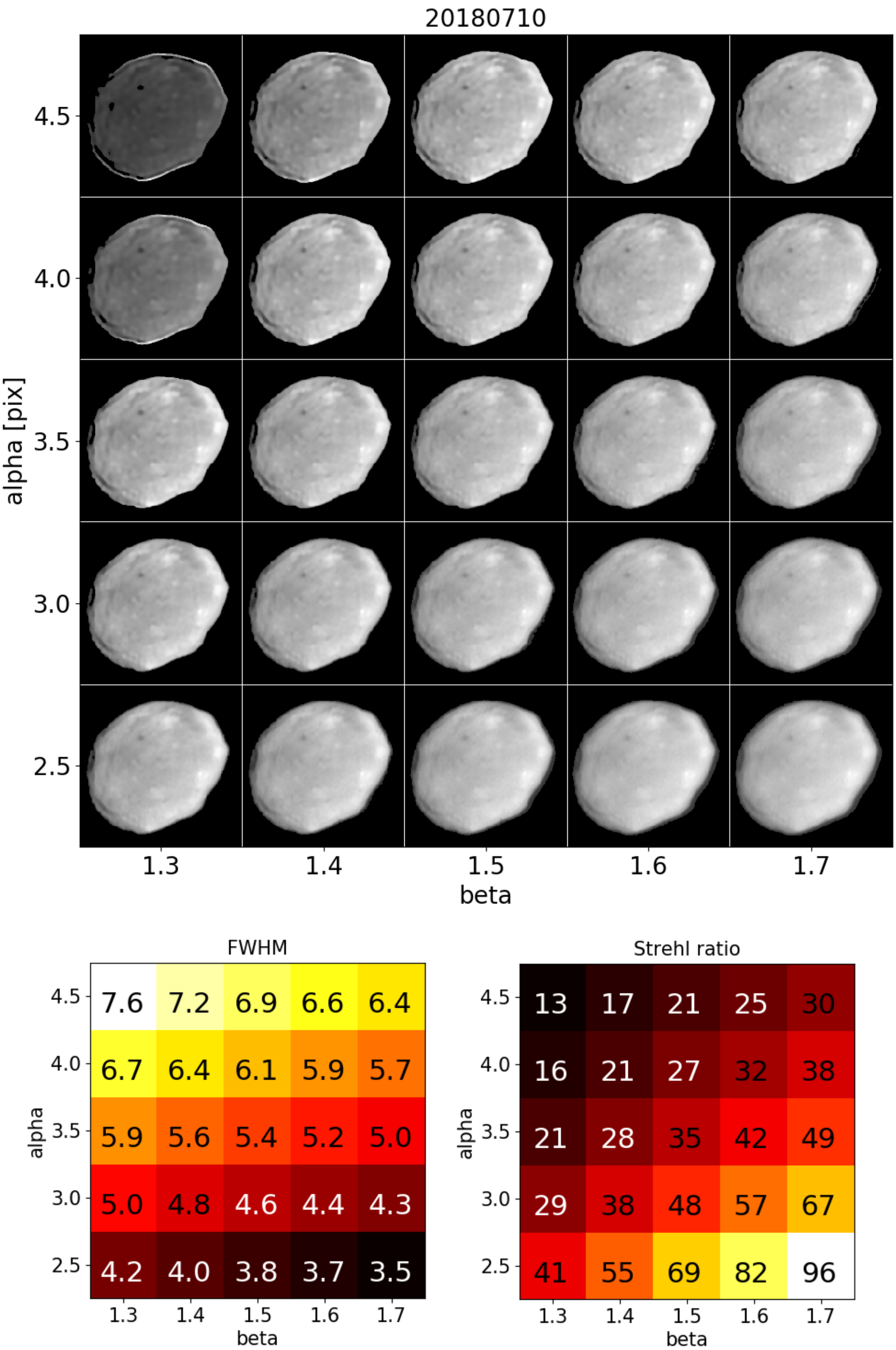

Fig. 2: Top: VLT/SPHERE/ZIMPOL observation on 2018 July 10$^{\rm th}$ deconvolved using 25 different Moffat parametric PSFs. Bottom: Corresponding FWHM and Strehl ratio for the 25 PSFs. Values indicate the FWHM and Strehl ratio respectively, while the colormap (dark for low values, white for high values) helps to visualise the diagonal trend discussed in the text.

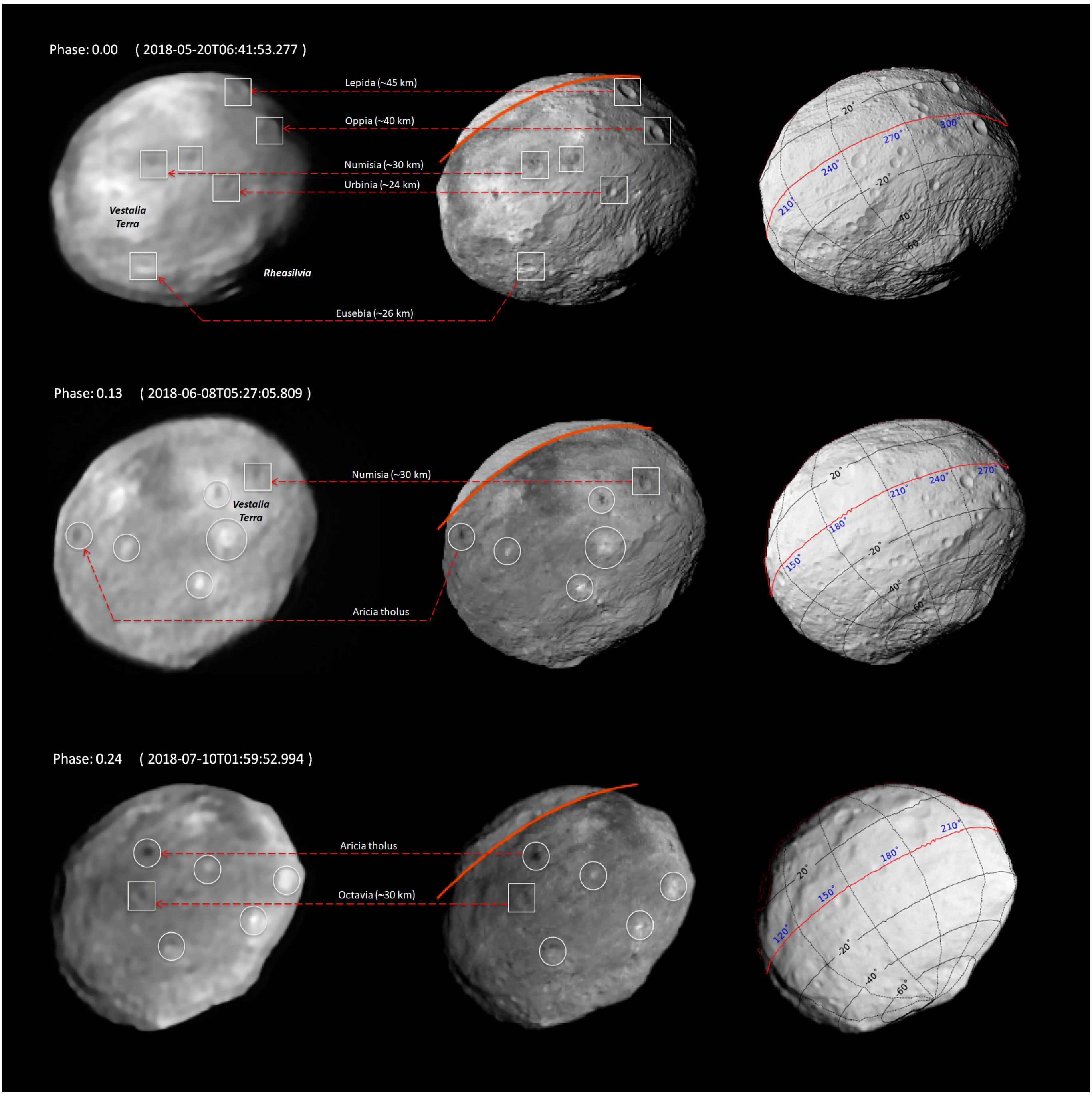

Fig. 3: Comparison of the VLT/SPHERE deconvolved images of Vesta (left) with synthetic projections of the Dawn model produced with OASIS and with albedo information from Schröder et al. (2014) (middle), and the same projection without albedo information but with a latitude/longitude coordinate grid for reference (right). All coordinates are given in the "Claudia" system (Russell et al. 2012). Note that no albedo data is available from Dawn for latitudes above $30°N$ (orange line). Finally, we highlight some of the main structures that can be identified in both the VLT/SPHERE images and the synthetic ones: craters are embedded in squares, and albedo features in circles. The first and second column images are displayed with a quadratic intensity scale to highlight the surface features.

4.1. OASIS synthetic images

The NASA/Dawn in situ mission provided high-resolution images of Vesta used to generate a global shape model (Preusker et al. 2016). The images also provided the rotational parameters of the objects with a high accuracy (Konopliv et al. 2014). Knowing the ephemeris of Vesta and the position of the Earth in the J2000 Equatorial frame, it is thus possible to generate unconvolved synthetic images of Vesta at the time of the SPHERE observations. We used the so-called "OASIS" tool (Jorda et al. 2010) developed and used in the frame of the Rosetta mission to create these images. The tool takes into account the pixel scale of the instrument, the viewing and illumination conditions of the object, its global shape, its rotational parameters

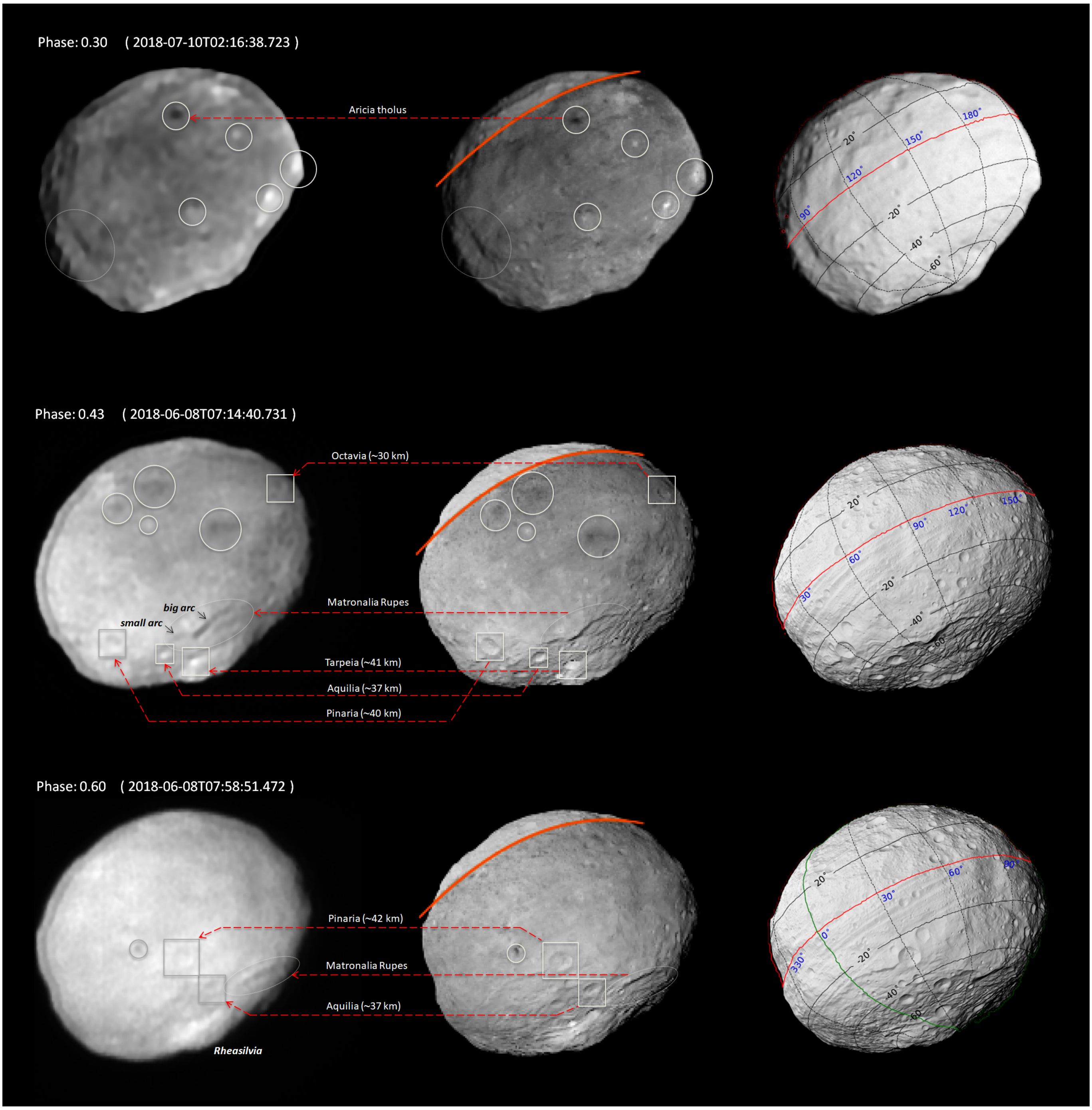

Fig. 3 *(continued)*

and the Hapke parameters describing its bi-directional reflectance properties. It rigorously accounts for cast shadows and considers the geometric intersection between the triangular facets of the shape model and the pixels to calculate pixel values. We used Hapke (1986)'s model with the parameters of Li et al. (2013) to describe the reflectance of the surface. These synthetic images represent the resolution limit that could have been achieved with a turbulent-less atmosphere and perfect optics.

4.2. Contour extraction and comparison

In order to perform a quantitative comparison between observed and synthetic (OASIS) images, we choose to perform a comparison between contour plots. Indeed contours are important for 3D shape reconstruction algorithms. The extraction of these contour plots was performed in several steps described below. For the observed images, a low threshold T_1 was estimated by fitting the histogram of the pixels in a box of 21×21 pixels around the minimum pixel of the image. For the synthetic images, the low threshold was set to zero. A high threshold T_2 was then calculated as the maximum pixel value after removing the 10 % highest

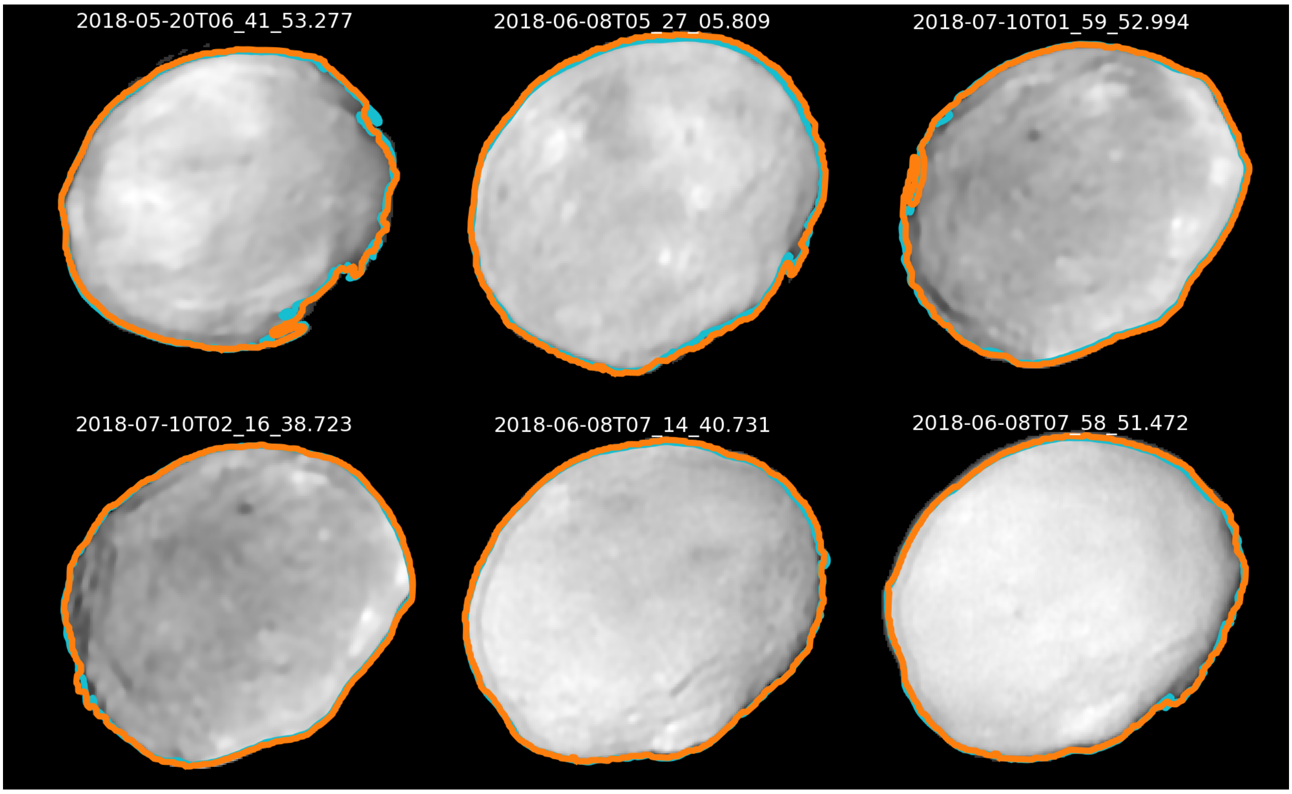

Fig. 4: Vesta contours computed for both the synthetic images produced with OASIS (light blue line) and the VLT/SPHERE ones after deconvolution (orange line). Contours are plotted over the VLT/SPHERE ones for comparison.

Epoch (UTC)	χ [pix]	χ_{Limb} [pix]	χ_{Term} [pix]	$\mathcal{A}_O$ [pix^2]	$\mathcal{A}_D$ [pix^2]
2018-05-20 06:41:53	0.83	0.41	0.99	19272	19414 (+0.73%)
2018-06-08 05:27:05	1.50	0.65	1.27	22673	23382 (+3.12%)
2018-06-08 07:14:40	0.55	0.40	0.54	22762	22920 (+0.70%)
2018-06-08 07:58:51	0.60	0.42	0.71	22362	22379 (+0.52%)
2018-07-10 01:59:52	1.37	0.39	1.73	21017	21224 (+0.98%)
2018-07-10 02:16:38	0.72	0.34	0.87	21223	21402 (+0.84%)
Average $^{\pm\text{std}}$	$0.93^{\pm 0.37}$	$0.44^{\pm 0.10}$	$1.02^{\pm 0.39}$		$(+1.15^{\pm 0.89}\%)$

Table 1: Results on the contour extraction for OASIS and deconvolved images. The χ, χ_{Limb} and χ_{Term} errors are explicited in the text. Columns $\mathcal{A}_O$ and $\mathcal{A}_D$ are respectively the area encircled by OASIS and deconvolution contours. Percentages inside parenthesis show the relative error on the estimated deconvolved area with respect to the OASIS area.

pixel values. The contour level to be used was defined as $T = T_1 + \zeta\,(T_2 - T_1)$, where ζ is a parameter in the interval $[0, 1]$ allowing to set the value of the contour level with respect to the high and low thresholds. Here $\zeta = 0.3$ has been chosen. The image was then converted into a triangular mesh. For this, the Cartesian coordinates of the vertices were defined by the coordinates $(X = i, Y = j)$ of the pixel (i, j), complemented by its value $Z = P_{ij}$. Each block of 2×2 pixels allowed to define two triangles. The resulting set of triangles allowed to represent the image as a triangular mesh. Finally, the intersection of the triangular mesh with the plane $Z = T$ defined the contour plot, represented here as a set of connected 2D points.

Let us call $\{D_i\}_{i \in [1,I]}$ and $\{M_j\}_{j \in [1,J]}$ respectively the set of points defining the deconvolved contour and the OASIS model contour. We defined the root mean square metric

$$\chi = \sqrt{\frac{\sum_i \lambda_i \cdot d(D_i, \{M_j\}_j)^2}{\sum_i \lambda_i}} \quad (4)$$

where the sum index i runs over all the contour points of the deconvolved image, $d(D_i, \{M_j\}_j)$ is the Euclidean distance between the point number i and its orthogonal projection onto the OASIS contour, λ_i is the pixel weighting factor. We choose λ_i to be the average distance between D_i and its neighbors D_{i-1} and D_{i+1} as

$$\lambda_i = \frac{1}{2}\left[d(D_i, D_{i-1}) + d(D_i, D_{i+1})\right] \quad (5)$$

so an eventual cluster of close points in the contour set doesn't induce highly localized weighting in the χ norm. Since the points are nearly homogeneously separated, the correction has small impact on the χ norm with respect to a simple weighting $\lambda_i = 1$. Finally,

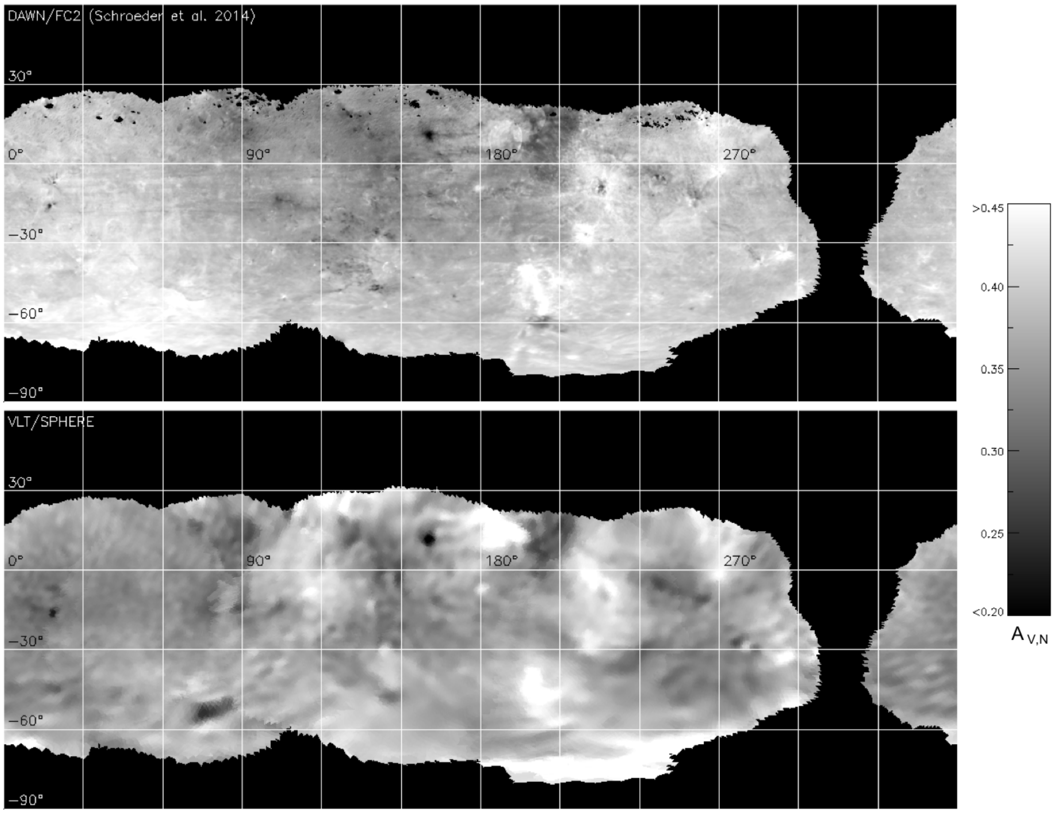

Fig. 5: Albedo map of Vesta constructed from VLT/SPHERE images (bottom), compared to the Dawn Framing Camera 2 (FC2) map derived in situ (top; Schröder et al. 2014). The two maps are in equidistant cylindrical projection. The Dawn map only shows the region of Vesta covered by SPHERE to facilitate the comparison. The North region of the Dawn map, with the latitude ϕ in the $[0°, +30°]$ range, contains several pixels with no available information. Those pixels are left black.

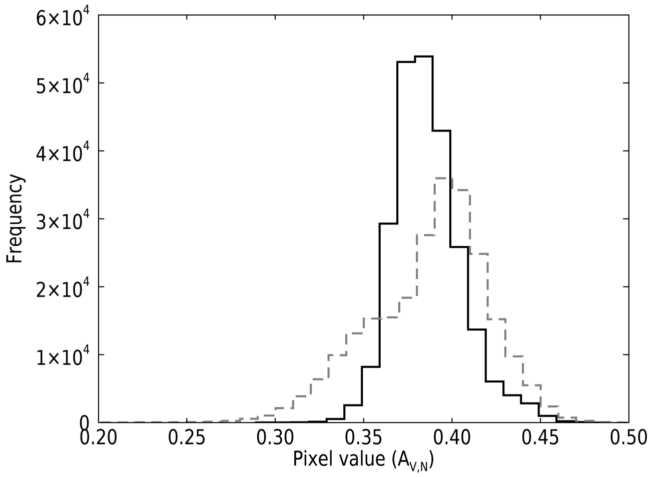

Fig. 6: Histogram of pixel values for the SPHERE (continuous black) and Dawn (dotted grey) albedo maps. The SPHERE map exhibits a slightly narrower range of albedo values with respect to Dawn, owing to its lower spatial resolution and residual blurring of the images due to imperfect deconvolution.

forcing $\lambda_i = 0$ for some points allows to select a specific area such as the limb or terminator for contour comparison.

Extraction of contours from the synthetic and deconvolved images show good agreement, see Fig. 4 for contour visualisation. The match between the contours is better at the limb ($\chi_{\rm Limb} = 0.44$ pixels) than at the terminator ($\chi_{\rm Term} = 1.02$ pixels). Indeed the OASIS facets illumination is much more sensitive to angular errors in the orientation of the facets for nearly tangent solar rays rather than normal rays. The average contour error, when taking into account all contour points, is $\chi = 0.93$ pixels, showing that sub-pixel contour resolution is achievable on asteroid deconvolved images.

The area encircled by the deconvolved contour is larger than the OASIS contour with a relative area difference of +1.15%. This error might be due to residual blurring not fully removed by the deconvolution and difficulties to extract the OASIS contour near the terminator. The resulting error on the volume would be $\sim +1.73\%$. All results concerning the contours are summarised in Table 1.

4.3. Reconnaissance of Vesta's main topographic features

It appears that most of the main topographic features present across Vesta's surface can already be recognised from the ground (Fig. 3). This includes the south pole impact basin and its prominent central mound, several D≥25 km sized craters and Matronalia Rupes including its steep scarp and its small and big arcs (Krohn et al. 2014). From these observations, we can determine a size limit of ∼30 km for the features that can be resolved with VLT/SPHERE (i.e. features, that are 8-10 pixels wide). Such detection limit should be in principle sufficient to recognise the North-South crater dichotomy detected by Dawn (Marchi et al. 2012; Vincent et al. 2014), according to the fact that the northern hemisphere hosts 70% of the craters with D≥30 km (Liu et al. 2018). There are several plausible explanations as to why we weren't able to resolve such dichotomy. First, we mostly imaged the southern hemisphere due to Vesta's spin axis orientation. Second, the atmospheric blurring (not entirely removed by the AO) is another limiting factor. Third, the albedo variegation across the surface is enormous, leading to a confusion between the shade of the craters and local albedo variation. This is well highlighted in the synthetic images generated with OASIS with and without albedo information (see middle and right column in Fig. 3). Finally, we do not observe the equatorial troughs of Vesta, that are 15 km wide and thus under the detection limit of our images. It follows that future generation telescopes with mirror sizes in the 30-40 m range should in principle be able to resolve the main features present across Vesta's surface, provided that they operate at the diffraction limit.

4.4. Reconnaissance of Vesta's main albedo features

To further test the reliability of the observation and deconvolution procedure, we built an albedo map of Vesta from the deconvolved SPHERE images, and compared this map to that of Schröder et al. (2014) from *in situ* Dawn measurements. We used a subsample of 19 high-quality images from the 6 epochs of VLT/SPHERE observations.

Owing to the limited number of geometrical views probed by SPHERE, it is not always possible to differentiate shadows from true albedo variations without prior knowledge about the local surface topography. Such information is very well constrained in the case of Vesta, and can be retrieved from the OASIS model. However, this is not true for most targets in our observing program, and for almost all asteroids in general. We therefore purposely did not use any prior information on Vesta's topography when building the map, in order to evaluate our ability to retrieve albedo information from the SPHERE observations only.

First, we corrected the illumination gradient of the SPHERE images, which depends on the local incidence, reflection, and phase angle. This was performed by fitting a second-order polynomial to the average disk of Vesta. This method provides satisfactory results for Earth-based observations of asteroids (Carry et al. 2008, 2010), when little is known about the local topography of the object. It provides better results than the use of a diffusion law (e.g., Lambert, Lommel-Seeliger) when no detailed 3D-shape model is available for the object. Using a diffusion law with a low-resolution shape model indeed results in artificially "paved" images owing to the resolution, i.e., the size of the facets, in the model. The use of a polynomial fit to the average disk of the object results in more realistic, smoother photometric correction. However, it cannot properly fit the illumination of local terrain features, such as craters and mountains.

For each SPHERE image, we then defined a Region Of Interest (ROI) containing the set of pixels to be projected on the map. As discussed in Section 3, an over-deconvolution usually enhances the brightness of the image regions with strong luminosity gradient, such as the asteroid border. To avoid including pixels affected by this effect, we considered only pixels contained in the central region of the asteroid, that is, typically 15-20 pixels away from the asteroid contour.

Next, the longitude and latitude of each pixel contained in the ROI was measured using a projection of the OASIS model (Section 4.1). For other targets in our program, this would be performed using a lower-resolution model derived with the ADAM software (Viikinkoski et al. 2015). Each pixel value was then projected on the map, using an equidistant cylindrical projection. The individual maps from the different epochs of observation were then combined together, using the overlapping regions to balance their brightness level. Finally, we normalised the combined map with the global average albedo of Vesta in the Johnson V-band (centred on 540 nm), in order to allow a direct comparison with the albedo map of Schröder et al. (2014).

The resulting map is shown and compared to that of Schröder et al. (2014) in Fig. 5. The Dawn map displays only the region of Vesta seen by SPHERE, in order to facilitate the comparison. Other pixels were set to zero.

The SPHERE map exhibits a wide range of albedo values (typically $A_{V,N}$=0.34–0.45), close to that of Dawn (mostly $A_{V,N}$=0.30–0.46), but slightly narrower owing to its lower spatial resolution and residual blurring due to imperfect deconvolution (Fig. 6). Most of the main albedo features present in the Dawn map can also be identified in the SPHERE one. We find that surface features down to 20-km in size can be identified from the SPHERE map.

Only a few inconsistencies between the two maps are found. The most obvious example consists in the presence of a dark region located near λ=80°, $\phi = -50°$ on the SPHERE map, whereas Dawn finds no such albedo variation at this location. Such feature most likely results from the presence of shadows in the SPHERE images caused by irregular terrains, rather than true albedo variations. The brightness of the southernmost region of Vesta on the map, for $\lambda \in [180°, 270°]$ and $\phi < -60°$ is enhanced with SPHERE compared to Dawn. This is due to the illumination of the Rheasilvia's central peak, that could not be accurately corrected. The Dawn map contains very localised regions with extremely low albedo values ($A_{V,N}$ <0.25). While those regions are also seen with SPHERE, they display higher albedos ($A_{V,N}$ >0.30) due to the lower spatial resolution of the map that attenuates the high-frequency albedo variations. Additional differences between the two maps may arise from the different filters used during the observations: ZIMPOL N_R (λ=589.2–702.6 nm) vs. DAWN FC2 clear filter (λ=438–965 nm).

4.5. Optimisation of the PSF parameters

Finally, in order to provide a direct visual comparison between VLT/SPHERE and Dawn, we projected the albedo map of Schröder et al. (2014) on the OASIS synthetic images (Figs. 3). By doing so, we were also able to determine the optimal values of α and β for the deconvolution by calculating the root square error between the deconvolved SPHERE/ZIMPOL images and the synthetic ones

(OASIS+albedo model). The error writes as

$$\epsilon(\alpha, \beta) = \sqrt{\sum_p (\mathrm{DEC}_p(\alpha, \beta) - a_p \cdot \mathrm{OAS}_p)^2} \quad (6)$$

where the sum runs over the pixels, OAS is the OASIS model, multiplied by the albedo a_p corresponding to each pixel, and DEC is our deconvolved image. When writing $\mathrm{DEC}_p(\alpha, \beta)$ we recall that the deconvolution depends on the PSF parameters (α, β). The minimisation of the error $\epsilon(\alpha, \beta)$ allows identifying the optimal values for the α and β parameters and thus the most accurate deconvolution in the sense of the norm given by Eq.6. Figure B.3 shows the evolution of ϵ with respect to the PSF parameters α and β for the 6 epochs. The minimum is reached in the narrow range $\alpha \simeq 3.5 - 4$ and $\beta \simeq 1.5 - 1.6$. Figure B.3 also shows that the error increases dramatically when the corona artefact appears, and that the minimum error is reached for sharp deconvolutions just before the corona effect.

Thus, the (α, β) parameters empirically estimated in Sec.3.2 are close to the actual optimal values that minimise the ϵ criteria. Near such optimal values, only the corona effect may corrupt the deconvolution result at high α and low β. Otherwise the deconvolution zone is stable since the deconvolution quality evolves continuously with the parameters (see Figs.2 and B.3).

Importantly, we believe that it is possible to further improve the deconvolution procedure using even more accurate PSF models, with a shape closer to that of the AO corrected PSF. Finally, PSF parameters (whatever the PSF model) may be estimated automatically by a myopic deconvolution algorithm, such as Mugnier et al. (2004) and Blanco & Mugnier (2011).

5. Conclusion

In this article, we evaluated how much topographic and albedo information can be retrieved from the ground with VLT/SPHERE in the case of the asteroid (4) Vesta. This object can be used as a benchmark for ground-based observations since the Dawn space mission provided us with ground truth information. We observed (4) Vesta with VLT/SPHERE/ZIMPOL as part of our ESO large program at six different epochs, and deconvolved the collected images with a parametric PSF. We then compared our VLT/SPHERE images with synthetic images of Vesta produced with the OASIS software that uses the 3D shape model of the Dawn mission as input and on which we re-projected the albedo map of the Dawn mission (Schröder et al. 2014). We further produced our own albedo map of Vesta from the SPHERE images alone, and without using any prior information about the surface topography of Vesta. We compared this map to that of Schröder et al. (2014) to evaluate our ability to differentiate true albedo variegation from shadows and regions with enhanced illumination due to imperfect photometric correction of the SPHERE images.

We show that the deconvolution of the VLT/SPHERE images with a parametric PSF allows retrieving the main topographic and albedo features present across Vesta's surface, down to a spatial resolution of ∼20–30 km. Contours extraction shows a precision of ∼1 pixel, with a strong difference between the estimation of the limb (precision of ∼0.5 pixel) and the terminator (precision of ∼1 pixel). The consequent relative error on the estimated area is $\leq 2\%$.

The present study demonstrates for the very first time the accuracy of ground-based AO imaging observations of asteroids with respect to *in situ* ones. Future generation telescopes (ELT, TMT, GMT) could use Vesta as a benchmark to catch all of the main features present across its surface (including the troughs and the North-South crater dichotomy), provided that these telescopes operate at the diffraction limit.

Acknowledgements. This work was supported by the French Direction Générale de l'Armement (DGA) and Aix-Marseille Université (AMU). P. Vernazza, A. Drouard, and B. Carry were supported by CNRS/INSU/PNP. J. Hanuš was supported by the grant 18-09470S of the Czech Science Foundation and by the Charles University Research program No. UNCE/SCI/023. This project has received funding from the European Union's Horizon 2020 research and innovation program under grant agreement No. 730890. This material reflects only the authors' views and the Commission is not liable for any use that may be made of the information contained therein. The authors thank S. Schröder for providing his reconstructed albedo map based on the Dawn images.

References

Andersen, D. R., Stoesz, J., Morris, S., et al. 2006, Publications of the Astronomical Society of the Pacific, 118, 1574
Beuzit, J.-L., Feldt, M., Dohlen, K., et al. 2008, in Ground-based and airborne instrumentation for astronomy II, Vol. 7014, International Society for Optics and Photonics, 701418
Blanco, L. & Mugnier, L. M. 2011, 19, 23227
Carry, B., Dumas, C., Fulchignoni, M., et al. 2008, A&A, 478, 235
Carry, B., Dumas, C., Kaasalainen, M., et al. 2010, Icarus, 205, 460
Conan, J.-M., Mugnier, L. M., Fusco, T., Michau, V., & Rousset, G. 1998, Applied Optics, 37, 4614
Fusco, T., Petit, C., Rousset, G., et al. 2006, in Proc. SPIE, Vol. 6272, Society of Photo-Optical Instrumentation Engineers (SPIE) Conference Series, 62720K
Fusco, T., Sauvage, J.-F., Mouillet, D., et al. 2016, in Proc. SPIE, Vol. 9909, Adaptive Optics Systems V, 99090U
Hapke, B. 1986, Icarus, 67, 264
Jaumann, R., Williams, D. A., Buczkowski, D. L., et al. 2012, Science, 336, 687
Jorda, L., Spjuth, S., Keller, H. U., Lamy, P., & Llebaria, A. 2010, in Proc. SPIE, Vol. 7533, Computational Imaging VIII, 753311
Konopliv, A. S., Asmar, S. W., Park, R. S., et al. 2014, Icarus, 240, 103
Krohn, K., Jaumann, R., Otto, K., et al. 2014, Icarus, 244, 120
Li, J.-Y., Le Corre, L., Schröder, S. E., et al. 2013, Icarus, 226, 1252
Liu, Z., Yue, Z., Michael, G., et al. 2018, Icarus, 311, 242
Marchi, S., McSween, H. Y., O'Brien, D. P., et al. 2012, Science, 336, 690
Marchis, F., Kaasalainen, M., Hom, E. F. Y., et al. 2006, Icarus, 185, 39
Moffat, A. 1969, Astronomy and Astrophysics, 3, 455
Mugnier, L. M., Fusco, T., & Conan, J.-M. 2004, JOSA A, 21, 1841
Preusker, F., Scholten, F., Matz, K.-D., et al. 2016, NASA Planetary Data System, 268, DAWN
Reddy, V., Nathues, A., Le Corre, L., et al. 2012, Science, 336, 700
Russell, C. T., Raymond, C. A., Coradini, A., et al. 2012, Science, 336, 684
Sánchez, F. M., Davies, R., Eisenhauer, F., et al. 2006, Astronomy & Astrophysics, 454, 481
Schenk, P., O'Brien, D. P., Marchi, S., et al. 2012, Science, 336, 694

Schmid, H.-M., Downing, M., Roelfsema, R., et al. 2012, in Ground-based and Airborne Instrumentation for Astronomy IV, Vol. 8446, International Society for Optics and Photonics, 84468Y
Schröder, S. E., Mottola, S., Keller, H. U., Raymond, C. A., & Russell, C. T. 2014, Planet. Space Sci., 103, 66
Thalmann, C., Schmid, H. M., Boccaletti, A., et al. 2008, in Ground-based and Airborne Instrumentation for Astronomy II, Vol. 7014, International Society for Optics and Photonics, 70143F
Thomas, P. C., Binzel, R. P., Gaffey, M. J., et al. 1997, Science, 277, 1492
Vernazza, P., Brož, M., Drouard, A., et al. 2018, A&A, 618, A154
Viikinkoski, M., Kaasalainen, M., & Durech, J. 2015, A&A, 576, A8
Viikinkoski, M., Vernazza, P., Hanuš, J., et al. 2018, A&A, 619, L3
Vincent, J.-B., Schenk, P., Nathues, A., et al. 2014, Planet. Space Sci., 103, 57

Appendix A: Observation table

Appendix B: Additional figures

OASIS including albedo is the intensity image of Vesta that should be observed by VLT/SPHERE/ZIMPOL in case of a perfect observation (no blurring due to pupil diffraction or atmosphere). Comparing pixel per pixel the intensities of the OASIS image and the deconvolved image intensities is then a metric of the deconvolved image quality. Figure B.2 shows the deconvolution pixels intensity with respect to that of the OASIS+albedo for the 6 different epochs of observation. Each intensity map has been normalised by its average. For each cloud of points the computed correlation between intensities is in the range 80% to 89%.

Table A.1: List of Vesta images. For each observation, the table gives the epoch, the telescope/instrument, the photometric filter, the exposure time, the airmass, the distance to the Earth Δ and the Sun r, the phase angle α, the angular diameter D_a and the reference or the PI of the AO project.

Date	UT	Instrument	Filter	Exp (s)	Airmass	Δ (AU)	r (AU)	α (°)	D_a (″)	Reference or PI
2018-05-20	6:41:53	VLT/SPHERE	N_R	80	1.01	1.25	2.15	15.8	0.579	Vernazza
2018-05-20	6:43:24	VLT/SPHERE	N_R	80	1.01	1.25	2.15	15.8	0.579	Vernazza
2018-05-20	6:44:56	VLT/SPHERE	N_R	80	1.01	1.25	2.15	15.8	0.579	Vernazza
2018-05-20	6:46:25	VLT/SPHERE	N_R	80	1.01	1.25	2.15	15.8	0.579	Vernazza
2018-05-20	6:47:56	VLT/SPHERE	N_R	80	1.01	1.25	2.15	15.8	0.579	Vernazza
2018-06-08	5:27:05	VLT/SPHERE	N_R	80	1.01	1.16	2.15	6.8	0.624	Vernazza
2018-06-08	5:28:36	VLT/SPHERE	N_R	80	1.01	1.16	2.15	6.8	0.624	Vernazza
2018-06-08	5:30:08	VLT/SPHERE	N_R	80	1.01	1.16	2.15	6.8	0.624	Vernazza
2018-06-08	5:31:38	VLT/SPHERE	N_R	80	1.00	1.16	2.15	6.8	0.624	Vernazza
2018-06-08	5:33:07	VLT/SPHERE	N_R	80	1.00	1.16	2.15	6.8	0.624	Vernazza
2018-06-08	7:14:40	VLT/SPHERE	N_R	80	1.08	1.16	2.15	6.7	0.624	Vernazza
2018-06-08	7:16:10	VLT/SPHERE	N_R	80	1.09	1.16	2.15	6.7	0.624	Vernazza
2018-06-08	7:17:42	VLT/SPHERE	N_R	80	1.09	1.16	2.15	6.7	0.624	Vernazza
2018-06-08	7:19:12	VLT/SPHERE	N_R	80	1.09	1.16	2.15	6.7	0.624	Vernazza
2018-06-08	7:20:41	VLT/SPHERE	N_R	80	1.10	1.16	2.15	6.7	0.624	Vernazza
2018-06-08	7:58:51	VLT/SPHERE	N_R	80	1.19	1.16	2.15	6.7	0.624	Vernazza
2018-06-08	8:00:22	VLT/SPHERE	N_R	80	1.19	1.16	2.15	6.7	0.624	Vernazza
2018-06-08	8:01:51	VLT/SPHERE	N_R	80	1.20	1.16	2.15	6.7	0.624	Vernazza
2018-06-08	8:03:21	VLT/SPHERE	N_R	80	1.20	1.16	2.15	6.7	0.624	Vernazza
2018-06-08	8:04:52	VLT/SPHERE	N_R	80	1.21	1.16	2.15	6.7	0.624	Vernazza
2018-07-10	1:59:52	VLT/SPHERE	N_R	80	1.04	1.19	2.16	10.9	0.608	Vernazza
2018-07-10	2:01:24	VLT/SPHERE	N_R	80	1.03	1.19	2.16	10.9	0.608	Vernazza
2018-07-10	2:02:56	VLT/SPHERE	N_R	80	1.03	1.19	2.16	10.9	0.608	Vernazza
2018-07-10	2:04:25	VLT/SPHERE	N_R	80	1.03	1.19	2.16	10.9	0.608	Vernazza
2018-07-10	2:05:56	VLT/SPHERE	N_R	80	1.03	1.19	2.16	10.9	0.608	Vernazza
2018-07-10	2:16:38	VLT/SPHERE	N_R	80	1.02	1.19	2.16	10.9	0.608	Vernazza
2018-07-10	2:18:09	VLT/SPHERE	N_R	80	1.02	1.19	2.16	10.9	0.608	Vernazza
2018-07-10	2:19:39	VLT/SPHERE	N_R	80	1.02	1.19	2.16	10.9	0.608	Vernazza
2018-07-10	2:21:09	VLT/SPHERE	N_R	80	1.02	1.19	2.16	10.9	0.608	Vernazza
2018-07-10	2:22:39	VLT/SPHERE	N_R	80	1.02	1.19	2.16	10.9	0.608	Vernazza

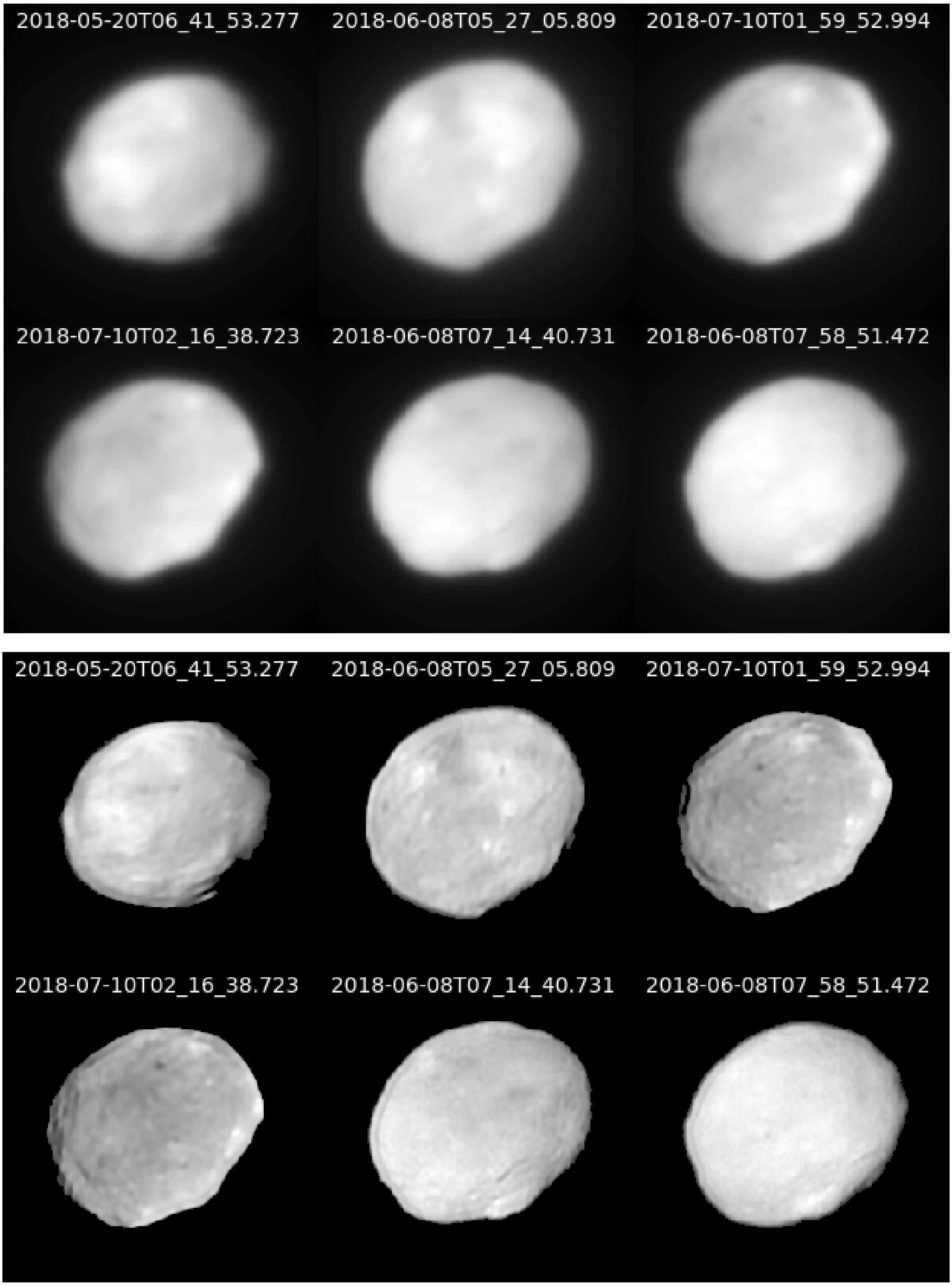

Fig. B.1: Top figure: reduced Vesta images after pipeline. Bottom figure: same images after deconvolution. Images are shown in the natural linear intensity scale.

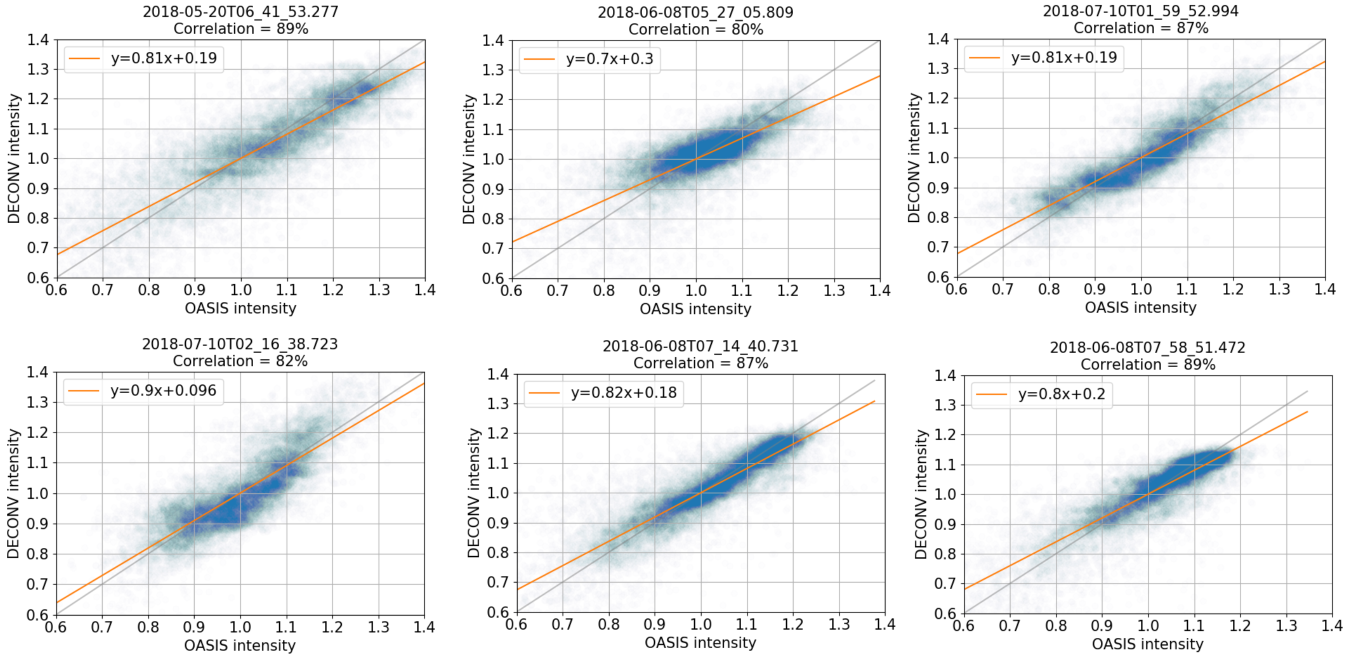

Fig. B.2: Correlation between OASIS (including albedo) and deconvolved images pixel intensities. Each intensity map has been divided by its average value for normalisation. Each of the 6 graphs corresponds to an epoch of observation. The linear fit of each cloud of points is also shown (orange line). The correlation percentage between OASIS and deconvolution intensities is written at the top of each graph.

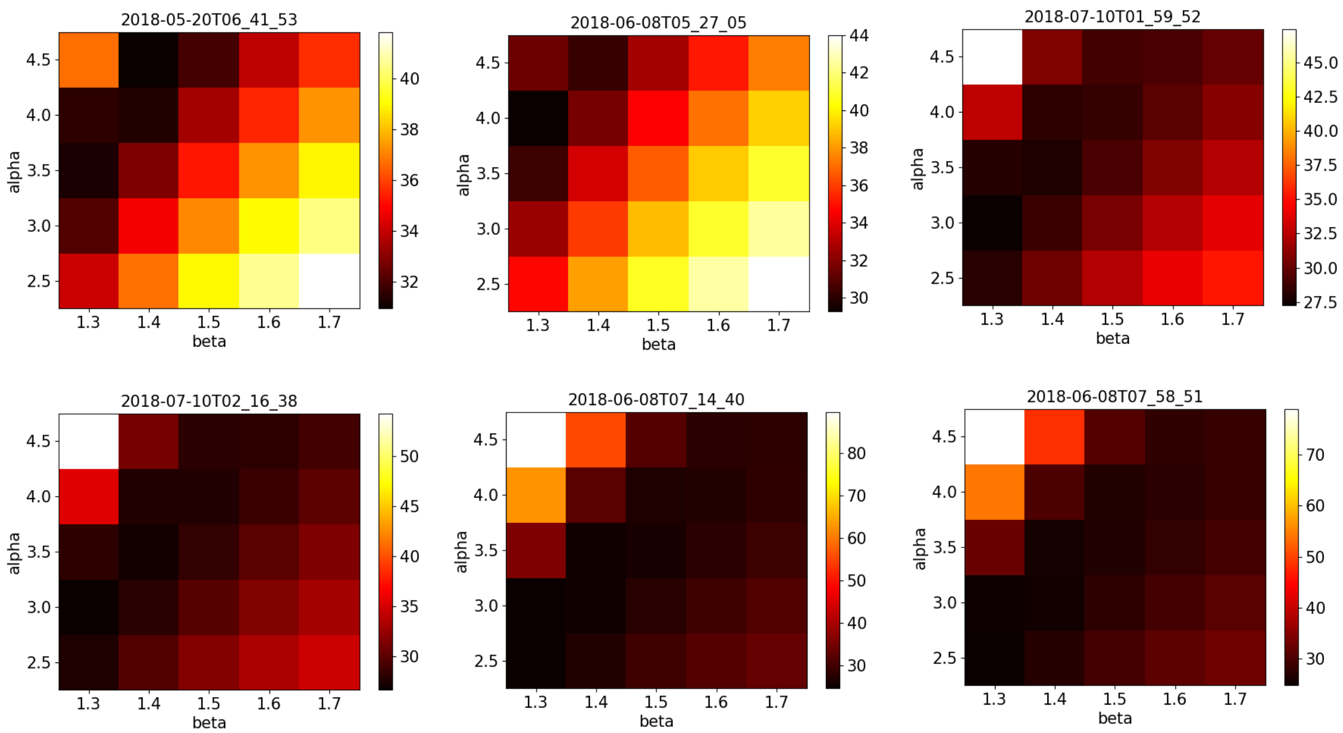

Fig. B.3: Root square error between deconvolved images and OASIS+albedo model. Each of the 6 subfigures corresponds to one of the observing epoch. Evolution of the error with respect to the α and β parameters is then visible. Invalid pixels (missing albedo) where removed for error computation. However all pixels (inside AND outside the asteroid) are considered to take into account the residual blurring after eventual incomplete deconvolution.